Frontiers of Information Technology & Electronic Engineering
www.jzus.zju.edu.cn; engineering.cae.cn; www.springerlink.com
ISSN 2095-9184 (print); ISSN 2095-9230 (online)
E-mail: jzus@zju.edu.cn

Robust wideband waveform design with constant modulus and discrete phase constraints for distributed precision jamming*

Qingsong ZHOU, Jialong QIAN, Zhongping YANG†‡, Chao HUANG,
Qinxian CHEN, Yibo XU, Zhengkai WEI

College of Electronic Engineering, National University of Defense Technology, Hefei 230037, China

†E-mail: yangzhongping14@nudt.edu.cn

Received Apr. 14, 2024; Revision accepted July 7, 2024; Crosschecked Nov. 15, 2024; Published online Dec. 27, 2024

Abstract: Distributed precision jamming (DPJ) is a novel blanket jamming concept in electronic warfare, which delivers the jamming resource to the opponent equipment precisely and ensures that friendly devices are not affected. Robust jamming performance and low hardware burden on the jammers are crucial for practical DPJ implementation. To achieve these goals, we study the robust design of wideband constant modulus (CM) discrete phase waveform for DPJ, where the worst-case combined power spectrum (CPS) of both the opponent and friendly devices is considered in the objective function, and the CM discrete phase constraints are used to design the wideband waveform. Specifically, the resultant mathematical model is a large-scale minimax multi-objective optimization problem (MOP) with CM and discrete phase constraints. To tackle the challenging MOP, we transform it into a single-objective minimization problem using the L_p-norm and Pareto framework. For the approximation problem, we propose the Riemannian conjugate gradient for CM discrete phase constraints (RCG-CMDPC) algorithm with low computational complexity, which leverages the complex circle manifold and a projection method to satisfy the CM discrete phase constraints within the RCG framework. Numerical examples demonstrate the superior robust DPJ effectiveness and computational efficiency compared to other competing algorithms.

Key words: Wideband waveform design; Constant modulus (CM); Discrete phase; Riemannian conjugate gradient (RCG); Distributed precision jamming (DPJ)
https://doi.org/10.1631/FITEE.2400285 **CLC number:** TN972

1 Introduction

For most electronic devices, the quality of service (QoS) highly depends on the signal-to-interference-plus-noise ratio (SINR) in practice (Wang et al., 2018; Gao et al., 2020; Geng et al., 2023). Therefore, blanket jamming is usually used in electronic warfare to degrade the QoS of these devices (Pärlin et al., 2021; Kelsey, 2023; Wu et al., 2023). Conventional blanket jamming is typically implemented by a single jammer, where a high power is required for jamming effectiveness but results in low utilization efficiency (Tai et al., 2016). Meanwhile, the beamforming technique is also usually used to enhance the transmit gain by directing the jamming energy toward two-dimensional (2D) directions. However, due to the insufficient dimensionality in the spatial domain, it may cause unexpected injuries to adjacent friendly devices in the three-dimensional (3D) area of interest (Li and Stoica, 2008; Blunt and Mokole, 2016). To overcome these problems, a novel blanket jamming concept, namely, distributed precision jamming (DPJ), was proposed by the US Defense Advanced Research Project Agency (https://www.fbo.gov/spg/ODA/DARPA/CMO/DARPA-BAA-09-65/listing.html). This method requires that

‡ Corresponding author
* Project supported by the National Natural Science Foundation of China (No. 62301581) and the Postgraduate Scientific Research Innovation Project of Hunan Province, China (No. CX20230045)
ORCID: Zhongping YANG, https://orcid.org/0000-0002-5881-0597

the opponent equipment is jammed precisely in the 3D spatial domain, and the adjacent friendly devices are not affected by the jammers. Compared to the transmit beamforming technique, in this technique, a group of distributed aerial platforms is adopted to improve the coherent synthesis efficiency. More importantly, DPJ exhibits excellent jamming energy performance within the desired 3D area rather than along specific 2D directions (Song D et al., 2016).

The existing research on DPJ falls into two distinct categories from the perspective of the transmitted signal model. One category adopts the narrowband signal model and regards the combined energy control performance as the main design metric. Chen et al. (2020) proposed an efficient method to design the single snapshot constant modulus (CM) transmit signals, and the grating lobes in the area of interest are mitigated to some extent. Yang ZP et al. (2022) jointly optimized the CM signals and the location of distributed platforms to improve the spatial energy control performance. Zhang KD et al. (2022b) proposed a method to endow the narrowband waveform with jamming characteristics by fitting the combined waveform with white noise, and Yang ZP et al. (2023) further improved the algorithm's performance in terms of both jamming and computational efficiency. Other research works, including those by Yang ZP et al. (2021), Xu et al. (2022), and Zhang KD et al. (2022a), designed the narrowband transmitted waveform to improve the DPJ performance based on previous works, and interested readers may refer to them.

The other category uses the wideband transmitted waveform for the jamming tasks, where the combined power spectrum (CPS) is considered as the design metric. Zhang KD et al. (2023) obtained the cross-spectral density matrices (CSDMs) of the waveform by maximizing the average CPS of the opponent equipment, and then the available wideband CM waveform was recovered by synthesizing the CSDMs and suppressing the CPS of friendly devices. To improve the robust performance and computational efficiency, Yang ZP et al. (2024) considered the worst-case CPS performance in DPJ. In this work, they maximized the minimum CPS of the opponent equipment, and the CPS of friendly devices was constrained under a specific threshold. Compared to narrowband waveforms, wideband waveforms are generally preferred because narrowband waveforms require precise prior frequency knowledge of the opponent equipment to execute spot jamming. Meanwhile, most previous works designed the CM continuous phase waveform, which makes it possible for the hardware component to operate in a saturation regime. From a practical point of view, CM waveforms should be designed with the discrete phase due to the limited number of bits in the direct digital synthesizer (DDS).

Compared to the narrowband jamming waveform, the advantages of the wideband jamming waveform lie in the following two aspects. First, due to detection errors on the working frequency of the opponent equipment, the wideband jamming waveform can cover the working frequency of the opponent equipment better, which has better robust jamming performance especially when the prior knowledge of reconnaissance is imprecise. Second, it is difficult for the antijamming system to suppress all the jamming frequency components from the view of the opponent equipment, making the jamming effect more significant than that of the narrowband jamming waveform. Even if the opponent equipment adopts the frequency-hopping waveform, the wideband jamming waveform can cover the range of frequency hopping, whereas the narrowband jamming waveform is invalid for this scenario. Therefore, the waveform for DPJ should be wideband to cover the potential working frequency of the opponent equipment. Note that the SINR is usually considered as the design metric to evaluate the antijamming effect from the view of opponent equipment. However, the opponent equipment and the jammers are noncooperative, which means that this metric cannot be obtained by the jammer to evaluate the jamming effect and design the waveform. The DPJ system usually accounts for the combined energy directly to evaluate the jamming effect, which is proportional to the SINR. In this case, the worst-case CPS of both the opponent and friendly devices is used to measure the robust jamming performance. Moreover, the wideband waveforms are required to be with CM and discrete phase to alleviate the hardware burden. Considering the numerous spatial frequency discrete points, our problem boils down to a large-scale minimax multi-objective optimization problem (MOP) with CM and discrete phase constraints, which requires an efficient algorithm with low computational complexity to generate real-time waveforms.

Though many methods have designed the waveform with CM and discrete phase constraints in the field of multiple-input multiple-output (MIMO) radar waveform design, most of them are oriented toward the narrowband signal model, where the problem size is much smaller than that of the wideband design. Zhao et al. (2017) used the majorization–minimization (MM) framework to design the low-autocorrelation CM discrete phase sequence. Pishrow and Abouei (2021) proposed a sequential rank-one constraint relaxation method to further minimize the autocorrelation function sidelobes by jointly designing the discrete phase transmit sequence and receive filter; however, the computational complexity of solving the convex problem at each iteration is too high to tackle the large-scale optimization problem. Lu et al. (2021) designed CM narrowband finite alphabet phase code by maximizing the signal-to-noise ratio, whereby a coordinate descent (CD) algorithm was proposed to improve the computational efficiency. Yang J et al. (2022) proposed an accelerated CD algorithm to design the narrowband CM discrete phase waveform for the low sidelobe beam pattern. Bu et al. (2021) proposed an inexact alternating direction penalty method framework to tackle optimization problems with quartic terms, where extra variables were introduced to split the original problem into two subproblems. However, the aforementioned methods are not suitable for our problem: the MM framework poses a high computational burden in addressing the large-scale optimization problem, while the other algorithms do not apply to the minimax MOP.

In this paper, we study the wideband CM discrete phase waveform design for DPJ. To guarantee robust jamming performance, we optimize the worst-case CPS of both the opponent and friendly devices to ensure DPJ effectiveness. The major contributions of this paper are summarized as follows:

1. A more practical wideband CM discrete phase waveform design model. Different from previous works on the narrowband CM discrete phase waveform design (Zhao et al., 2017; Bu et al., 2021; Lu et al., 2021; Pishrow and Abouei, 2021; Yang J et al., 2022), we use the wideband signal model to design the CM discrete phase waveform for DPJ, which is more suitable for jamming and has lower requirement on the hardware components in practice (Yang ZP et al., 2024). To guarantee robust jamming performance, we optimize the worst-case CPS performance of both the opponent and friendly devices, whereby the formulated problem boils down to a large-scale minimax MOP with CM and discrete phase constraints.

2. A novel low-complexity algorithm to tackle the optimization problem with CM and discrete phase constraints. To tackle the resultant nonconvex NP-hard problem, we simplify the problem using the L_p-norm, and the approximation problem aims to minimize the p-power terms with CM and discrete phase constraints. Unlike the current manifold optimization, which can deal with only the problem with CM constraints (Absil et al., 2008; Manton, 2020), we propose a novel Riemannian conjugate gradient for CM discrete phase constraints (RCG-CMDPC) algorithm to address our large-scale approximation problem, where the algorithm is developed within the complex circle manifold and a projection method to satisfy both the CM and discrete phase constraints.

3. Numerical simulation insights and detailed validation. The performance of the proposed RCG-CMDPC algorithm is demonstrated under a typical DPJ scenario. Numerical examples are implemented to show that RCG-CMDPC exhibits lower computational complexity and better jamming efficiency compared with state-of-the-art MM algorithm, which makes it possible to generate real-time wideband CM discrete phase waveform for DPJ. Moreover, we analyze the effect of the hyperparameters on the performance of the RCG-CMDPC algorithm and give the Pareto curve of the worst-case CPSs between the opponent and friendly devices.

Notations: Vectors and matrices are denoted by lowercase and uppercase boldface letters, respectively. The i^{th} element of vector $\boldsymbol{x}$ is represented by $\boldsymbol{x}_i$. $\mathbb{C}^N$ and $\mathbb{R}^N$ denote the sets of N-dimensional complex and real fields, respectively. $\|\boldsymbol{x}\|$ denotes the Euclidean norm of vector $\boldsymbol{x}$, and $\arg(\boldsymbol{x})$ represents the argument of complex number $\boldsymbol{x}$. $\mathrm{Tr}(\boldsymbol{X})$, $\mathrm{rank}(\boldsymbol{X})$, and $\lambda_{\max}(\boldsymbol{X})$ are the trace, rank, and the maximum eigenvalue of matrix $\boldsymbol{X}$, respectively. $(\cdot)^*$, $(\cdot)^{\mathrm{T}}$, and $(\cdot)^{\mathrm{H}}$ denote the complex conjugate, transpose, and conjugate transpose, respectively. $\boldsymbol{I}_M$ and $\boldsymbol{0}_M$ denote the $M \times M$ identity matrix and $M \times 1$ zero vector, respectively. $\odot$ and $\otimes$ represent the Hadamard and Kronecker products, respectively.

2 Problem formulation

2.1 Signal model

For the scenario of interest in this paper, the DPJ system consists of M drones as shown in Fig. 1, where the location of the m^{th} drone is denoted as $\boldsymbol{r}_m$, m=1, 2, ⋯, M, with M denoting the number of drones in the DPJ system. The drones are distributed randomly in an ultrasparse manner, which means that the distance between any two drones is much greater than the half-wavelength. Suppose that the opponent equipment and friendly devices are located within the area of interest Ω, the opponent region Ω_{O} is assumed as a circle that involves the opponent equipment, and the w^{th} friendly device is located in the w^{th} circle friendly region Ω_{F}^{w}, w=1, 2,⋯W, with W being the number of friendly devices. To avoid prior information errors on the location of these devices and the ensuing need for robustness, the DPJ system should achieve high CPS in Ω_{O} for the blanket jamming action and control the CPS in Ω_{F}^{w} at a low level.

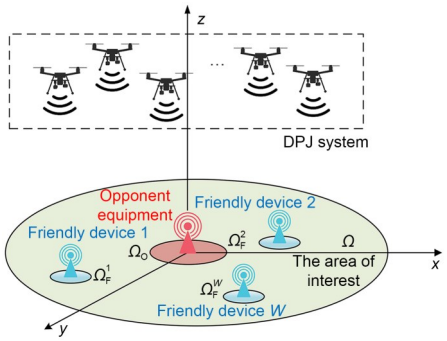

Fig. 1 Blanket jamming action implemented by the distributed precision jamming (DPJ) system consisting of M drones

Let each jammer of the DPJ system be equipped with a single antenna, and let the m^{th} jammer radiate a distinct baseband signal $\boldsymbol{x}_m(t)$ with bandwidth B, where the spectral support is in the interval [−B/2, B/2]. Thus, the combined signal at any point $\boldsymbol{\sigma}_z$ in the area of interest Ω can be expressed as follows (Zhang KD et al., 2023):

$$s_z(t)=\sum_{m=1}^{M}\boldsymbol{x}_m\left(t-\tau_m(\boldsymbol{\sigma}_z)\right)\frac{\mathrm{e}^{\mathrm{j}2\pi f_0\left(t-\tau_m(\boldsymbol{\sigma}_z)\right)}}{\left\|\boldsymbol{r}_m-\boldsymbol{\sigma}_z\right\|_2}, \tag{1}$$

where f_0 is the carrier frequency, $\tau_m(\boldsymbol{\sigma}_z)=\left\|\boldsymbol{r}_m-\boldsymbol{\sigma}_z\right\|_2/c$ is the propagation time, and c is the speed of light. Note that these distributed unmanned aerial vehicles (UAVs) are assumed to be calibrated perfectly; i.e., the localization and synchronization errors are not taken into account, which is a typical assumption in the research on the distributed platform (Liu et al., 2022; Zeng et al., 2023; Tan et al., 2024). When adopting digital signal processing techniques, the sampled baseband signal is represented by $\boldsymbol{x}_m(n)=\boldsymbol{x}_m(t)\big|_{t=nT_{\text{s}}}(n=1, 2, \cdots, N)$, where $T_{\text{s}}=1/B$ is the sampling interval, n denotes the particular sample number, and N is the total number of samples. Thus, the discrete Fourier transform (DFT) of $\boldsymbol{x}_m(n)$ is given by Eq. (2):

$$y_m(q)=\frac{1}{\sqrt{N}}\sum_{n=1}^{N}\boldsymbol{x}_m(n)\mathrm{e}^{-\mathrm{j}2\pi\frac{(n-1)q}{N}}, q\in\left\{-\frac{N}{2},\frac{N}{2}-1\right\}. \tag{2}$$

To facilitate the following derivation, the sampled baseband signal $\left\{\boldsymbol{x}_m(n)\,\middle|\,n=1, 2, \cdots, N\right\}$ is vectorized by $\boldsymbol{x}_m=\left[\boldsymbol{x}_m(1),\boldsymbol{x}_m(2),\cdots,\boldsymbol{x}_m(N)\right]^{\mathrm{T}}$, and thus $y_m(q)$ can be rewritten as follows:

$$y_m(q)=\boldsymbol{x}_m^{\mathrm{T}}\boldsymbol{f}_q, \tag{3}$$

where $\boldsymbol{f}_q=\left[1, \mathrm{e}^{-\mathrm{j}2\pi q/N}, \cdots, \mathrm{e}^{-\mathrm{j}2\pi(N-1)q/N}\right]^{\mathrm{T}}/\sqrt{N}$. In the same manner, by implementing N-point DFT on the sampled form of Eq. (1), we deconstruct the steering vector of the spatial point $\boldsymbol{\sigma}_z$ with respect to the discrete frequency grid frequency q for the wideband signal as follows (Yang ZP et al., 2024):

$$\boldsymbol{a}_{\boldsymbol{\sigma}_z,q}=\left[\frac{\mathrm{e}^{\mathrm{j}2\pi\left(qB/N+f_0\right)\tau_1(\boldsymbol{\sigma}_z)}}{\left\|\boldsymbol{r}_1-\boldsymbol{\sigma}_z\right\|_2},\ldots,\frac{\mathrm{e}^{\mathrm{j}2\pi\left(qB/N+f_0\right)\tau_M(\boldsymbol{\sigma}_z)}}{\left\|\boldsymbol{r}_M-\boldsymbol{\sigma}_z\right\|_2}\right]^{\mathrm{T}}. \tag{4}$$

Therefore, based on Eqs. (1)–(4), the CPS at the spatial frequency point $(\boldsymbol{\sigma}_z, q)$ is given by Eq. (5):

$$\boldsymbol{P}_{\boldsymbol{\sigma}_z,q}=\left|\boldsymbol{a}_{\boldsymbol{\sigma}_z,q}^{\mathrm{H}}\boldsymbol{y}_q\right|^2=\left|\boldsymbol{a}_{\boldsymbol{\sigma}_z,q}^{\mathrm{H}}\boldsymbol{F}_q\boldsymbol{x}\right|^2=\boldsymbol{x}^{\mathrm{H}}\boldsymbol{\Pi}_{\boldsymbol{\sigma}_z,q}\boldsymbol{x}, \tag{5}$$

where $\boldsymbol{y}_q=\left[y_1(q),y_2(q),\cdots,y_M(q)\right]^{\mathrm{T}}$, $\boldsymbol{F}_q=\left(\boldsymbol{f}_q^{\mathrm{T}}\otimes\boldsymbol{I}_M\right)\in\mathbb{C}^{M\times MN}$, $\boldsymbol{x}=\left[\boldsymbol{x}_1^{\mathrm{T}},\boldsymbol{x}_2^{\mathrm{T}},\cdots,\boldsymbol{x}_M^{\mathrm{T}}\right]^{\mathrm{T}}\in\mathbb{C}^{MN}$, and $\boldsymbol{\Pi}_{\boldsymbol{\sigma}_z,q}=\boldsymbol{F}_q^{\mathrm{H}}\boldsymbol{a}_{\boldsymbol{\sigma}_z,q}\cdot\boldsymbol{a}_{\boldsymbol{\sigma}_z,q}^{\mathrm{H}}\boldsymbol{F}_q$ is defined as the steering matrix of the spatial frequency point $(\boldsymbol{\sigma}_z, q)$.

2.2 Metric and waveform constraint design

To guarantee robust wideband DPJ effectiveness, we optimize the minimum and maximum CPSs among all the spatial frequency points of the opponent equipment and friendly devices, and the corresponding design metrics are formulated as follows:

$$\begin{cases} f_1(\boldsymbol{x}) = \min\limits_{\boldsymbol{\sigma}_{\mathrm{O}} \in \Omega_{\mathrm{O}}, q_{\mathrm{O}} \in \Xi_{\mathrm{O}}} \boldsymbol{x}^{\mathrm{H}} \boldsymbol{\Pi}_{\boldsymbol{\sigma}_{\mathrm{O}}, q_{\mathrm{O}}} \boldsymbol{x} \\ \qquad = \max\limits_{\boldsymbol{\sigma}_{\mathrm{O}} \in \Omega_{\mathrm{O}}, q_{\mathrm{O}} \in \Xi_{\mathrm{O}}} -\boldsymbol{x}^{\mathrm{H}} \boldsymbol{\Pi}_{\boldsymbol{\sigma}_{\mathrm{O}}, q_{\mathrm{O}}} \boldsymbol{x}, \\ f_2(\boldsymbol{x}) = \max\limits_{\boldsymbol{\sigma}_{\mathrm{F}} \in \Omega_{\mathrm{F}}, q_{\mathrm{F}} \in \Xi_{\mathrm{F}}} \boldsymbol{x}^{\mathrm{H}} \boldsymbol{\Pi}_{\boldsymbol{\sigma}_{\mathrm{F}}, q_{\mathrm{F}}} \boldsymbol{x}, \end{cases} \tag{6}$$

where $\Omega_{\mathrm{F}}=\Omega_{\mathrm{F}}^1 \cup \Omega_{\mathrm{F}}^2 \cup \cdots \cup \Omega_{\mathrm{F}}^W$ is the union of all the W friendly regions, and $\boldsymbol{\sigma}_{\mathrm{O}}$ and $\boldsymbol{\sigma}_{\mathrm{F}}$ represent the discrete spatial points in Ω_{O} and Ω_{F}, respectively. Meanwhile, q_{O} and q_{F} denote the discrete frequency points in the frequency bands Ξ_{O} and Ξ_{F} of opponent and friendly devices, respectively.

Next, we further give the constraints that the waveform $\boldsymbol{x}$ should satisfy. To avoid waveform distortion when the amplifiers work at the saturation condition (Aubry et al., 2020; Zhang JD and Xu, 2020; Fan T et al., 2024) and to adhere to the sufficient utilization of the limited jamming resource (Qiu et al., 2023; Yang ZP et al., 2023; Shi et al., 2024), we impose the CM constraint on waveform $\boldsymbol{x}$, which is given by Eq. (7):

$$\left|\boldsymbol{x}_i\right| = 1,\ i = 1, 2, \cdots, MN. \tag{7}$$

For the phase part of waveform $\boldsymbol{x}$, a limited number of bits are available in the DDS (Zhang WJ et al., 2020; Song YX et al., 2022), and thus the finite alphabet (i.e., discrete phase) constraint is enforced on $\boldsymbol{x}$ as follows:

$$\arg(\boldsymbol{x}_i) \in \Psi_V = \frac{2\pi}{V}[0,1,\cdots,V-1],\ i=1, 2, \cdots, MN, \tag{8}$$

where $V=2^v$ is the cardinality of the finite alphabet, and v is the number of bits in the DDS. In general, as v increases, it allows for more precise phases and a higher degree of freedom in the waveform $\boldsymbol{x}$. However, the DDS incurs a heavier hardware burden and higher cost on the jammer. It needs to be emphasized that the actual DDS cannot generate the waveform with an arbitrary (continuous) phase. Meanwhile, directly performing the quantization of continuous phase waveform devised by the above metric and CM constraints does not guarantee a desirable solution, which may trap the final waveform into local optimality or even cause severe performance losses in practice (Fan T et al., 2021; Imani and Nayebi, 2021; Yang J et al., 2022). Thus, it is of great significance to attach the waveform with discrete phase constraints as presented in Eq. (8).

2.3 Optimization problem

Based on the design metrics and waveform constraints, we formulate the minimax MOP as follows:

$$\begin{aligned} \mathcal{P}\begin{cases} \min\limits_{\boldsymbol{x}} \max\limits_{\boldsymbol{\sigma}_{\mathrm{O}} \in \Omega_{\mathrm{O}}, q_{\mathrm{O}} \in \Xi_{\mathrm{O}}} -\boldsymbol{x}^{\mathrm{H}} \boldsymbol{\Pi}_{\boldsymbol{\sigma}_{\mathrm{O}}, q_{\mathrm{O}}} \boldsymbol{x} \\ \min\limits_{\boldsymbol{x}} \max\limits_{\boldsymbol{\sigma}_{\mathrm{F}} \in \Omega_{\mathrm{F}}, q_{\mathrm{F}} \in \Xi_{\mathrm{F}}} \boldsymbol{x}^{H} \boldsymbol{\Pi}_{\boldsymbol{\sigma}_{\mathrm{F}}, q_{\mathrm{F}}} \boldsymbol{x} \end{cases} \\ \text{s.t. } \left|\boldsymbol{x}_i\right| = 1,\ i=1, 2, \cdots, MN, \\ \arg(\boldsymbol{x}_i) \in \Psi_V,\ i=1, 2, \cdots, MN. \end{aligned} \tag{9}$$

It is seen that $\mathcal{P}$ is a nonconvex, nonsmooth, and NP-hard problem due to the objective function and constraints, which makes it challenging to obtain the solution directly. Meanwhile, the abundant discrete points in the spatial and frequency domains result in a large-scale optimization problem, which causes great trouble in real-time waveform generation.

3 Algorithm design

In this section, we propose the RCG-CMDPC algorithm to obtain the wideband CM discrete phase waveform for robust DPJ effectiveness. First, we use L_p approximation and the Pareto optimization framework to transform the original minimax MOP $\mathcal{P}$ into a single-objective minimization problem with CM and discrete phase constraints. Then, the transformed problem is tackled by our proposed RCG-CMDPC algorithm, wherein the complex circle manifold is used, and the corresponding retraction methods are modified to satisfy the CM discrete phase constraints within the RCG framework. Finally, we provide the computational complexity analysis of the proposed RCG-CMDPC algorithm.

3.1 The problem transformation on $\mathcal{P}$

Inspired by the research on designing waveforms with low autocorrelation sidelobes (Song JX et al., 2016), we approximate the design metrics $f_1(\boldsymbol{x})$ and $f_2(\boldsymbol{x})$ using the L_p-norm to simplify the original problem $\mathcal{P}$. The inner term is required to be positive when applying the L_p-norm approximation. Thus, we transform the first term regarding $f_1(\boldsymbol{x})$ to a strictly positive term $C-f_1(\boldsymbol{x})$ by introducing the upper bound C of $f_1(\boldsymbol{x})$, where the maximization on $-f_1(\boldsymbol{x})$ is equivalent to that on $C-f_1(\boldsymbol{x})$. In this case, we have the expression of C as follows:

$$C=\max_{\boldsymbol{\sigma}_{\mathrm{O}}\in\Omega_{\mathrm{O}},q_{\mathrm{O}}\in\Xi_{\mathrm{O}}}\lambda_{\max}(\boldsymbol{\Pi}_{\boldsymbol{\sigma}_{\mathrm{O}},q_{\mathrm{O}}})MN\geq\max_{\boldsymbol{\sigma}_{\mathrm{O}}\in\Omega_{\mathrm{O}},q_{\mathrm{O}}\in\Xi_{\mathrm{O}}}\boldsymbol{x}^{\mathrm{H}}\boldsymbol{\Pi}_{\boldsymbol{\sigma}_{\mathrm{O}},q_{\mathrm{O}}}\boldsymbol{x}. \tag{10}$$

The inequality holds true by the fact that $\boldsymbol{x}^{\mathrm{H}}\boldsymbol{\Pi}_{\boldsymbol{\sigma}_{\mathrm{O}},q_{\mathrm{O}}}\boldsymbol{x}\leq\boldsymbol{x}^{\mathrm{H}}\lambda_{\max}(\boldsymbol{\Pi}_{\boldsymbol{\sigma}_{\mathrm{O}},q_{\mathrm{O}}})\boldsymbol{I}_{MN}\boldsymbol{x}=\lambda_{\max}(\boldsymbol{\Pi}_{\boldsymbol{\sigma}_{\mathrm{O}},q_{\mathrm{O}}})MN$. As discussed by Yang ZP et al. (2024), the constant C has the closed-form expression as follows:

$$C=\max_{\boldsymbol{\sigma}_{\mathrm{O}}\in\Omega_{\mathrm{O}}}\sum_{m=1}^{M}\frac{MN^2}{\left\|\boldsymbol{r}_m-\boldsymbol{\sigma}_{\mathrm{O}}\right\|_2}. \tag{11}$$

With the constant C at hand, the original problem $\mathcal{P}$ is recast as follows:

$$\mathcal{P}\begin{cases}\min\limits_{\boldsymbol{x}}\ \max\limits_{\boldsymbol{\sigma}_{\mathrm{O}}\in\Omega_{\mathrm{O}},q_{\mathrm{O}}\in\Xi_{\mathrm{O}}}C-\boldsymbol{x}^{\mathrm{H}}\boldsymbol{\Pi}_{\boldsymbol{\sigma}_{\mathrm{O}},q_{\mathrm{O}}}\boldsymbol{x}\\ \min\limits_{\boldsymbol{x}}\ \max\limits_{\boldsymbol{\sigma}_{\mathrm{F}}\in\Omega_{\mathrm{F}},q_{\mathrm{F}}\in\Xi_{\mathrm{F}}}\boldsymbol{x}^{\mathrm{H}}\boldsymbol{\Pi}_{\boldsymbol{\sigma}_{\mathrm{F}},q_{\mathrm{F}}}\boldsymbol{x}\\ \text{s.t. }\left|\boldsymbol{x}_i\right|=1,\ i=1,2,\cdots,MN,\\ \quad\arg(\boldsymbol{x}_i)\in\Psi_V,\ i=1,2,\cdots,MN,\end{cases} \tag{12}$$

where the equivalence between Eqs. (9) and (12) results from the identical solution for the maximization of $-\boldsymbol{x}^{\mathrm{H}}\boldsymbol{\Pi}_{\boldsymbol{\sigma}_{\mathrm{O}},q_{\mathrm{O}}}\boldsymbol{x}$ and $C-\boldsymbol{x}^{\mathrm{H}}\boldsymbol{\Pi}_{\boldsymbol{\sigma}_{\mathrm{O}},q_{\mathrm{O}}}\boldsymbol{x}$. By using the L_p-norm on the inner maximization operation, we obtain the approximated MOP as follows:

$$\mathcal{P}'\begin{cases}\min\limits_{\boldsymbol{x}}\left(\sum\limits_{\boldsymbol{\sigma}_{\mathrm{O}}\in\Omega_{\mathrm{O}}}\sum\limits_{q_{\mathrm{O}}\in\Xi_{\mathrm{O}}}\left(C-\boldsymbol{x}^{\mathrm{H}}\boldsymbol{\Pi}_{\boldsymbol{\sigma}_{\mathrm{O}},q_{\mathrm{O}}}\boldsymbol{x}\right)^p\right)^{1/p}\\ \min\limits_{\boldsymbol{x}}\left(\sum\limits_{\boldsymbol{\sigma}_{\mathrm{F}}\in\Omega_{\mathrm{F}}}\sum\limits_{q_{\mathrm{F}}\in\Xi_{\mathrm{F}}}\left(\boldsymbol{x}^{\mathrm{H}}\boldsymbol{\Pi}_{\boldsymbol{\sigma}_{\mathrm{F}},q_{\mathrm{F}}}\boldsymbol{x}\right)^p\right)^{1/p}\\ \text{s.t. }\left|\boldsymbol{x}_i\right|=1,\ i=1,2,\cdots,MN,\\ \quad\arg(\boldsymbol{x}_i)\in\Psi_V,\ i=1,2,\cdots,MN,\end{cases} \tag{13}$$

where the L_p-norm tends to be the original maximization (L_∞-norm) problem when $p\to\infty$. As $(\cdot)^{1/p}$ is a monotonic function in the domain of definition, the power of $1/p$ in the two objective functions can be ignored, and the approximated MOP is equivalently represented by the following expression:

$$\mathcal{P}'\begin{cases}\min\limits_{\boldsymbol{x}}\sum\limits_{\boldsymbol{\sigma}_{\mathrm{O}}\in\Omega_{\mathrm{O}}}\sum\limits_{q_{\mathrm{O}}\in\Xi_{\mathrm{O}}}\left(C-\boldsymbol{x}^{\mathrm{H}}\boldsymbol{\Pi}_{\boldsymbol{\sigma}_{\mathrm{O}},q_{\mathrm{O}}}\boldsymbol{x}\right)^p\\ \min\limits_{\boldsymbol{x}}\sum\limits_{\boldsymbol{\sigma}_{\mathrm{F}}\in\Omega_{\mathrm{F}}}\sum\limits_{q_{\mathrm{F}}\in\Xi_{\mathrm{F}}}\left(\boldsymbol{x}^{\mathrm{H}}\boldsymbol{\Pi}_{\boldsymbol{\sigma}_{\mathrm{F}},q_{\mathrm{F}}}\boldsymbol{x}\right)^p\\ \text{s.t. }\left|\boldsymbol{x}_i\right|=1,\ i=1,2,\cdots,MN,\\ \quad\arg(\boldsymbol{x}_i)\in\Psi_V,\ i=1,2,\cdots,MN.\end{cases} \tag{14}$$

To proceed, we apply the Pareto framework to transform $\mathcal{P}'$ to the following single-objective minimization problem:

$$\begin{aligned}\tilde{\mathcal{P}}:\ \min_{\boldsymbol{x}}\ f_\rho(\boldsymbol{x})=&\rho\sum_{\boldsymbol{\sigma}_{\mathrm{O}}\in\Omega_{\mathrm{O}}}\sum_{q_{\mathrm{O}}\in\Xi_{\mathrm{O}}}\left(C-\boldsymbol{x}^{\mathrm{H}}\boldsymbol{\Pi}_{\boldsymbol{\sigma}_{\mathrm{O}},q_{\mathrm{O}}}\boldsymbol{x}\right)^p\\ &+(1-\rho)\sum_{\boldsymbol{\sigma}_{\mathrm{F}}\in\Omega_{\mathrm{F}}}\sum_{q_{\mathrm{F}}\in\Xi_{\mathrm{F}}}\left(\boldsymbol{x}^{\mathrm{H}}\boldsymbol{\Pi}_{\boldsymbol{\sigma}_{\mathrm{F}},q_{\mathrm{F}}}\boldsymbol{x}\right)^p\\ \text{s.t. }\left|\boldsymbol{x}_i\right|=&\ 1,\ i=1,2,\cdots,MN,\\ \arg(\boldsymbol{x}_i)\in&\ \Psi_V,\ i=1,2,\cdots,MN,\end{aligned} \tag{15}$$

where $\rho\in[0,1]$ is the Pareto weight that is determined by the practical trade-offs between two objectives.

3.2 The proposed RCG-CMDPC algorithm for $\tilde{\mathcal{P}}$

In this subsection, we propose a novel RCG-CMDPC algorithm to tackle the transformed minimization problem $\tilde{\mathcal{P}}$ within the RCG framework. The geometrical structure of the complex circle manifold makes it possible to avoid some saddle points and achieve considerable convergence speed, and interested readers may refer to Manton (2020). In essence, manifold optimization is a gradient-based method in a particular space, where the original constrained problem is considered an unconstrained problem within the specific manifold.

3.2.1 Complex circle manifold and Riemannian metric

To make the description clear, we present the geometric interpretations of the complex circle manifold and the projection to the CM discrete phase constraints in Fig. 2, where the blue spherical surface

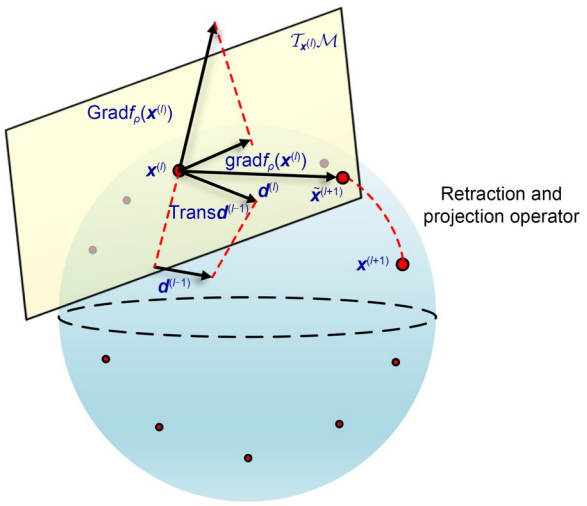

Fig. 2 Geometric interpretations of the complex circle manifold $\mathcal{M}$, where the red points appear on the spherical surface of the complex circle and possess discrete phases. References to color refer to the online version of this figure

denotes the complex circle manifold, and the red points are the discrete phases. As the modulus and phase parts for each $\boldsymbol{x}_i$ are independent, we give the set of points satisfying the CM constraints consisting of the proposed manifold $\mathcal{M}$ as follows:

$$\mathcal{M}=\left\{\boldsymbol{x}\in\mathbb{C}^{MN}\middle|\,|\boldsymbol{x}_i|=1,\,i=1,2,\cdots,MN\right\}. \tag{16}$$

For the discrete phase constraints, we quantize the solution at each iteration by a projection method, which is illustrated in the following section, and thus the manifold optimization can be implemented by temporarily leaving out the discrete phase constraints. In this case, the constrained problem $\tilde{\mathcal{P}}$ is viewed as an unconstrained problem over the manifold $\mathcal{M}$.

Compared with the Euclidean space, $\mathcal{M}$ is a particular space endowed with a local Euclidean structure; namely, any point $\boldsymbol{x}\in\mathcal{M}$ can be implemented only with Euclidean operation locally around itself. Suppose that $\boldsymbol{x}^{(l)}$ is the obtained point at the l^{th} iteration; we introduce the tangent space $\mathcal{T}_{\boldsymbol{x}^{(l)}}\mathcal{M}$, which contains all the tangent vectors of $\boldsymbol{x}^{(l)}$, and we represent $\mathcal{T}_{\boldsymbol{x}^{(l)}}\mathcal{M}$ by the light yellow surface in Fig. 2. To update $\boldsymbol{x}^{(l+1)}$ within the RCG framework, we need to specify a Riemannian metric for $\mathcal{M}$, which defines the product operation in the manifold. One common choice is the following Euclidean inner product (Absil et al., 2008):

$$\langle\boldsymbol{\xi},\boldsymbol{\eta}\rangle=\mathrm{Re}\{\boldsymbol{\xi}^{\mathrm{H}}\boldsymbol{\eta}\}, \tag{17}$$

where $\boldsymbol{\xi}$ and $\boldsymbol{\eta}$ are the tangent vectors on $\mathcal{T}_{\boldsymbol{x}^{(l)}}\mathcal{M}$.

3.2.2 Computation of the Riemannian gradient

To implement Euclidean operation on the current point $\boldsymbol{x}^{(l)}$, the corresponding Riemannian gradient $\mathrm{grad}f_\rho(\boldsymbol{x}^{(l)})$ is defined as a tangent vector through $\boldsymbol{x}^{(l)}$, which is the unique element with the fastest decrease of $f_\rho(\boldsymbol{x}^{(l)})$ such that

$$\left\langle\boldsymbol{\xi},\mathrm{grad}f_\rho(\boldsymbol{x}^{(l)})\right\rangle=\mathrm{D}f_\rho(\boldsymbol{x}^{(l)})[\boldsymbol{\xi}], \tag{18}$$

where $\mathrm{D}f_\rho(\boldsymbol{x}^{(l)})[\boldsymbol{\xi}]$ is the directional derivative of $f_\rho(\boldsymbol{x}^{(l)})$ at $\boldsymbol{x}^{(l)}$ in the direction $\boldsymbol{\xi}$. Therefore, the Riemannian gradient $\mathrm{grad}f_\rho(\boldsymbol{x}^{(l)})$ is regarded as the orthogonal projection of its Euclidean gradient $\mathrm{Grad}f_\rho(\boldsymbol{x}^{(l)})$ to $\mathcal{T}_{\boldsymbol{x}^{(l)}}\mathcal{M}$, as shown in Fig. 2. As discussed by Absil et al. (2008), the generalized projection operator of a point $\boldsymbol{u}$ to the tangent space of $\boldsymbol{v}$ is given by Eq. (19):

$$\mathrm{Proj}_{\mathcal{T}_{\boldsymbol{v}}\mathcal{M}}(\boldsymbol{u})=\boldsymbol{u}-\boldsymbol{v}\odot\mathrm{Re}\{\boldsymbol{u}\odot\boldsymbol{v}^*\}. \tag{19}$$

Thus, the Riemannian gradient $\mathrm{grad}f_\rho(\boldsymbol{x}^{(l)})$ is represented by

$$\begin{aligned}\mathrm{grad}f_\rho(\boldsymbol{x}^{(l)})&=\mathrm{Proj}_{\mathcal{T}_{\boldsymbol{x}^{(l)}}\mathcal{M}}\left(\mathrm{Grad}f_\rho(\boldsymbol{x}^{(l)})\right)\\&=\mathrm{Grad}f_\rho(\boldsymbol{x}^{(l)})-\boldsymbol{x}^{(l)}\odot\mathrm{Re}\left\{\mathrm{Grad}f_\rho(\boldsymbol{x}^{(l)})\odot\boldsymbol{x}^{(l)*}\right\},\end{aligned} \tag{20}$$

where $\mathrm{Grad}f_\rho(\boldsymbol{x}^{(l)})$ is derived as follows:

$$\begin{aligned}\mathrm{Grad}f_\rho(\boldsymbol{x}^{(l)})=&-2\rho\sum_{\sigma_{\mathrm{O}}\in\Omega_{\mathrm{O}}}\sum_{q_{\mathrm{O}}\in\Xi_{\mathrm{O}}}p\left(C-\boldsymbol{x}^{(l)\mathrm{H}}\boldsymbol{\Pi}_{\sigma_{\mathrm{O}},q_{\mathrm{O}}}\boldsymbol{x}^{(l)}\right)^{p-1}\\&\cdot\left(\boldsymbol{\Pi}_{\sigma_{\mathrm{O}},q_{\mathrm{O}}}\boldsymbol{x}^{(l)}\right)\\&+2(1-\rho)\sum_{\sigma_{\mathrm{F}}\in\Omega_{\mathrm{F}}}\sum_{q_{\mathrm{F}}\in\Xi_{\mathrm{F}}}p\left(\boldsymbol{x}^{(l)\mathrm{H}}\boldsymbol{\Pi}_{\sigma_{\mathrm{F}},q_{\mathrm{F}}}\boldsymbol{x}^{(l)}\right)^{p-1}\\&\cdot\left(\boldsymbol{\Pi}_{\sigma_{\mathrm{F}},q_{\mathrm{F}}}\boldsymbol{x}^{(l)}\right).\end{aligned} \tag{21}$$

3.2.3 The RCG framework and projection to the CM discrete phase constraints

To proceed, we adopt the RCG framework to update $\boldsymbol{x}^{(l+1)}$. Similar to the conjugate gradient algorithm in Euclidean space, the RCG algorithm combines with the last descent direction $\boldsymbol{d}^{(l-1)}$ for the current update direction $\boldsymbol{d}^{(l)}$, which is given as follows:

$$\boldsymbol{d}^{(l)} = -\mathrm{grad} f_\rho(\boldsymbol{x}^{(l)}) + \mu^{(l)} \mathrm{Trans}\boldsymbol{d}^{(l-1)}. \tag{22}$$

Compared to the common conjugate gradient algorithm in Euclidean space, the last descent direction $\boldsymbol{d}^{(l-1)}$ in the RCG algorithm needs be projected to $\mathcal{T}_{\boldsymbol{x}^{(l)}}\mathcal{M}$ for the local Euclidean operations around $\boldsymbol{x}^{(l)}$. Thus, $\mathrm{Trans}\boldsymbol{d}^{(l-1)}$ in Eq. (22) is expressed as follows:

$$\begin{aligned}\mathrm{Trans}\boldsymbol{d}^{(l-1)} &= \mathrm{Proj}_{\mathcal{T}_{\boldsymbol{x}^{(l)}}\mathcal{M}}(\boldsymbol{d}^{(l-1)}) \\ &= \boldsymbol{d}^{(l-1)} - \boldsymbol{x}^{(l)} \odot \mathrm{Re}\{\boldsymbol{d}^{(l-1)} \odot \boldsymbol{x}^{(l)*}\},\end{aligned} \tag{23}$$

and $\mu^{(l)}$ is the Polak–Ribière parameter for the generalized conjugate gradient algorithm such that (Boumal, 2014)

$$\mu^{(l)} = \frac{\left\langle \mathrm{grad} f_\rho(\boldsymbol{x}^{(l)}), \mathrm{grad} f_\rho(\boldsymbol{x}^{(l)}) - \mathrm{Proj}_{\mathcal{T}_{\boldsymbol{x}^{(l)}}\mathcal{M}}\left(\mathrm{grad} f_\rho(\boldsymbol{x}^{(l-1)})\right)\right\rangle}{\left\langle \mathrm{grad} f_\rho(\boldsymbol{x}^{(l-1)}), \mathrm{grad} f_\rho(\boldsymbol{x}^{(l-1)})\right\rangle}. \tag{24}$$

For the clear derivation, we introduce the following updated intermediate variable to represent the updated vector on the tangent space $\mathcal{T}_{\boldsymbol{x}^{(l)}}\mathcal{M}$:

$$\tilde{\boldsymbol{x}}^{(l+1)} = \boldsymbol{x}^{(l)} + \zeta^{(l)}\boldsymbol{d}^{(l)}, \tag{25}$$

where $\zeta^{(l)}$ is the step size of the descent direction, which is determined by the back tracking-Armijo line-search method, and the corresponding expression is given subsequently.

In what follows, we introduce the retraction operation and the projection method, which ensure that the updated point satisfies the CM discrete phase constraints. Differing from the retraction that operates only the modulus of $\boldsymbol{x}^{(l)}$ in the complex circle manifold, we define the retraction and projection operator $\Re(\cdot)$, which projects both the modulus and the phase parts of $\boldsymbol{x}^{(l)}$, and the updated $\boldsymbol{x}^{(l+1)}$ is expressed as follows:

$$\begin{cases}\boldsymbol{x}^{(l+1)} = \Re\left(\tilde{\boldsymbol{x}}^{(l+1)}\right) = \left[\mathrm{e}^{\mathrm{j}\hat{\varphi}_1}, \mathrm{e}^{\mathrm{j}\hat{\varphi}_2}, \cdots, \mathrm{e}^{\mathrm{j}\hat{\varphi}_{MN}}\right]^{\mathrm{T}}, \\ \hat{\varphi}_i = \dfrac{2\pi}{V}\left\lfloor \dfrac{\arg(\hat{\boldsymbol{x}}_i^{(l+1)})}{2\pi/V}\right\rfloor,\end{cases} \tag{26}$$

with $\lfloor\cdot\rfloor$ denoting the biggest integer not larger than itself. This retraction and projection method ensures that $\tilde{\boldsymbol{x}}^{(l+1)}$ is projected to satisfy the CM discrete phase constraints at each iteration within the RCG framework.

Then, the expression of the parameter $\zeta^{(l)}$ in Eq. (25) is as follows (Absil et al., 2008):

$$\begin{cases}\zeta^{(l)} = \alpha^k \beta, \\ f_\rho(\boldsymbol{x}^{(l)}) - f_\rho\left(\Re(\tilde{\boldsymbol{x}}^{(l+1)})\right) \geq -\delta\left\langle \mathrm{grad} f_\rho(\boldsymbol{x}^{(l)}), \zeta^{(l)}\boldsymbol{d}^{(l)}\right\rangle,\end{cases} \tag{27}$$

where $\alpha=0.5$, $\beta=1\Big/\left\|\mathrm{grad} f_\rho \boldsymbol{x}^{(l)}\right\|$, and $\delta=0.5$ are a group of classic parameters in the Armijo line-search method, and k is the smallest nonnegative integer such that Eq. (27) is satisfied.

Finally, we summarize the RCG-CMDPC algorithm for our problem $\tilde{\mathcal{P}}$ in Algorithm 1, and it terminates when the absolute variation of $f_\rho(\boldsymbol{x})$ satisfies the stopping criterion.

Algorithm 1 The proposed RCG-CMDPC algorithm for tackling $\tilde{\mathcal{P}}$

Input: Initial point $\boldsymbol{x}^{(0)} \in \mathcal{M}$

Output: The optimal solution $\boldsymbol{x}^{(\mathrm{opt})} \in \mathcal{M}$

Initialize $l=1$
Compute $\boldsymbol{d}^{(0)} = -\mathrm{grad} f_\rho(\boldsymbol{x}^{(0)})$ and the step size $\zeta^{(0)}$
Obtain the intermediate variable $\tilde{\boldsymbol{x}}^{(1)} = \boldsymbol{x}^{(0)} + \zeta^{(0)}\boldsymbol{d}^{(0)}$, and update $\boldsymbol{x}^{(1)} = \Re(\tilde{\boldsymbol{x}}^{(0)})$
Repeat
    Compute the Riemannian gradient $\mathrm{grad} f_\rho(\boldsymbol{x}^{(l)})$ using Eqs. (20) and (21)
    Calculate the Polark–Ribière parameter $\mu^{(l)}$ using Eq. (24)
    Update $\boldsymbol{d}^{(l)}$ and $\mathrm{Trans}\boldsymbol{d}^{(l-1)}$ using Eqs. (22) and (23), respectively
    Compute the step size $\zeta^{(l)}$ by Armijo's back tracking method in Eq. (27)
    Update $\tilde{\boldsymbol{x}}^{(l+1)} = \boldsymbol{x}^{(l)} + \zeta^{(l)}\boldsymbol{d}^{(l)}$
    Implement retraction and update $\boldsymbol{x}^{(l+1)} = \Re(\tilde{\boldsymbol{x}}^{(l+1)})$ using Eq. (26)
    Let $l=l+1$
until $\left|f_\rho(\boldsymbol{x}^{(l+1)}) - f_\rho(\boldsymbol{x}^{(l)})\right| \Big/ f_\rho(\boldsymbol{x}^{(l)}) \leq \varepsilon$, then output $\boldsymbol{x}^{(\mathrm{opt})} = \boldsymbol{x}^{(l)}$

3.3 Complexity analysis of the proposed RCG-CMDPC algorithm

Though most of the update procedures in Algorithm 1 involve projection operations, the computational complexity remains linear with $O(MN)$ due to the

selected Riemannian metric. However, the computational complexity of grad$f_\rho(\boldsymbol{x}^{(l)})$ and $\zeta^{(l)}$ is high due to the costly computation of Grad$f_\rho(\boldsymbol{x}^{(l)})$ and $f_\rho(\boldsymbol{x}^{(l)})$, respectively. To alleviate the computational burden on the algorithm, we give an equivalent computation of $f_\rho(\boldsymbol{x}^{(l)})$ as follows:

$$\begin{aligned} f_\rho(\boldsymbol{x}^{(l)}) &= f_\rho(\boldsymbol{X}^{(l)}) \\ &= \rho \sum_{\boldsymbol{\sigma}_{\mathrm{O}} \in \Omega_{\mathrm{O}}} \sum_{q_{\mathrm{O}} \in \Xi_{\mathrm{O}}} \left(C - \boldsymbol{f}_{q_{\mathrm{O}}}^{\mathrm{H}} (\boldsymbol{X}^{(l)})^{\mathrm{H}} \boldsymbol{a}_{\boldsymbol{\sigma}_{\mathrm{O}}, q_{\mathrm{O}}} \boldsymbol{a}_{\boldsymbol{\sigma}_{\mathrm{O}}, q_{\mathrm{O}}}^{\mathrm{H}} \boldsymbol{X}^{(l)} \boldsymbol{f}_{q_{\mathrm{O}}} \right)^p \\ &\quad + (1-\rho) \sum_{\boldsymbol{\sigma}_{\mathrm{F}} \in \Omega_{\mathrm{F}}} \sum_{q_{\mathrm{F}} \in \Xi_{\mathrm{F}}} \left(\boldsymbol{f}_{q_{\mathrm{F}}}^{\mathrm{H}} (\boldsymbol{X}^{(l)})^{\mathrm{H}} \boldsymbol{a}_{\boldsymbol{\sigma}_{\mathrm{F}}, q_{\mathrm{F}}} \boldsymbol{a}_{\boldsymbol{\sigma}_{\mathrm{F}}, q_{\mathrm{F}}}^{\mathrm{H}} \boldsymbol{X}^{(l)} \boldsymbol{f}_{q_{\mathrm{F}}} \right)^p, \end{aligned} \tag{28}$$

where $\boldsymbol{X}^{(l)} \in \mathbb{C}^{M \times N}$ is the matrix form of $\boldsymbol{x}^{(l)}$ by reshaping every N elements of $\boldsymbol{x}^{(l)}$ as a row of $\boldsymbol{X}^{(l)}$ in order, while $\boldsymbol{f}_{q_{\mathrm{O}}}$ and $\boldsymbol{f}_{q_{\mathrm{F}}}$ satisfy $\boldsymbol{F}_{q_{\mathrm{O}}} = \boldsymbol{f}_{q_{\mathrm{O}}}^{\mathrm{T}} \otimes \boldsymbol{I}_M$ and $\boldsymbol{F}_{q_{\mathrm{F}}} = \boldsymbol{f}_{q_{\mathrm{F}}}^{\mathrm{T}} \otimes \boldsymbol{I}_M$, respectively, as presented in Section 2. Compared with the original form, the computational complexity of $f_\rho(\boldsymbol{x}^{(l)})$ is reduced from $O\left((U_{\mathrm{O}}Q_{\mathrm{O}} + U_{\mathrm{F}}Q_{\mathrm{F}})M^2N\right)$ to $O\left((U_{\mathrm{O}}Q_{\mathrm{O}} + U_{\mathrm{F}}Q_{\mathrm{F}})MN\right)$ significantly, where U_{O} and U_{F} are the numbers of discrete spatial points in Ω_{O} and Ω_{F}, while Q_{O} and Q_{F} are the numbers of discrete frequency points in Ξ_{O} and Ξ_{F}, respectively.

In the same manner, we rewrite the Euclidean gradient Grad$f_\rho(\boldsymbol{x}^{(l)})$ as the following equivalent form:

$$\begin{aligned} \mathrm{Grad} f_\rho(\boldsymbol{X}^{(l)}) &= -2\rho \sum_{\boldsymbol{\sigma}_{\mathrm{O}} \in \Omega_{\mathrm{O}}} \boldsymbol{F}_{q_{\mathrm{O}}}^{\mathrm{H}} \\ &\cdot \left(\sum_{q_{\mathrm{O}} \in \Xi_{\mathrm{O}}} p (C - \boldsymbol{f}_{q_{\mathrm{O}}}^{\mathrm{H}} (\boldsymbol{X}^{(l)})^{\mathrm{H}} \boldsymbol{a}_{\boldsymbol{\sigma}_{\mathrm{O}}, q_{\mathrm{O}}} \boldsymbol{a}_{\boldsymbol{\sigma}_{\mathrm{O}}, q_{\mathrm{O}}}^{\mathrm{H}} \boldsymbol{X}^{(l)} \boldsymbol{f}_{q_{\mathrm{O}}})^{p-1} \right. \\ &\cdot \left. \left((\boldsymbol{a}_{\boldsymbol{\sigma}_{\mathrm{O}}, q_{\mathrm{O}}}^{\mathrm{H}} \boldsymbol{X}^{(l)} \boldsymbol{f}_{q_{\mathrm{O}}}) \boldsymbol{a}_{\boldsymbol{\sigma}_{\mathrm{O}}, q_{\mathrm{O}}} \right) \right) \\ &\quad + 2(1-\rho) \sum_{\boldsymbol{\sigma}_{\mathrm{F}} \in \Omega_{\mathrm{F}}} \boldsymbol{F}_{q_{\mathrm{F}}}^{\mathrm{H}} \\ &\cdot \left(\sum_{q_{\mathrm{F}} \in \Xi_{\mathrm{F}}} p \left(\boldsymbol{f}_{q_{\mathrm{F}}}^{\mathrm{H}} (\boldsymbol{X}^{(l)})^{\mathrm{H}} \boldsymbol{a}_{\boldsymbol{\sigma}_{\mathrm{F}}, q_{\mathrm{F}}} \boldsymbol{a}_{\boldsymbol{\sigma}_{\mathrm{F}}, q_{\mathrm{F}}}^{\mathrm{H}} \boldsymbol{X}^{(l)} \boldsymbol{f}_{q_{\mathrm{F}}} \right)^{p-1} \right. \\ &\cdot \left. \left((\boldsymbol{a}_{\boldsymbol{\sigma}_{\mathrm{F}}, q_{\mathrm{F}}}^{\mathrm{H}} \boldsymbol{X}^{(l)} \boldsymbol{f}_{q_{\mathrm{F}}}) \boldsymbol{a}_{\boldsymbol{\sigma}_{\mathrm{F}}, q_{\mathrm{F}}} \right) \right), \end{aligned} \tag{29}$$

where the computational complexity is highly decreased from $O\left((U_{\mathrm{O}}Q_{\mathrm{O}} + U_{\mathrm{F}}Q_{\mathrm{F}})(M^2N^2 + M^2N)\right)$ to $O\left((U_{\mathrm{O}}Q_{\mathrm{O}} + U_{\mathrm{F}}Q_{\mathrm{F}})MN + (U_{\mathrm{O}} + U_{\mathrm{F}})M^2N\right)$.

To sum up, we give the computational complexity of the proposed RCG-CMDPC algorithm in Table 1, while—as customary—disregarding the coefficients of high-order terms.

Table 1 Computational complexity summary of the RCG-CMDPC algorithm

Computation	Complexity
Grad$f_\rho(\boldsymbol{x}^{(l)})$	$O\left((U_{\mathrm{O}}Q_{\mathrm{O}} + U_{\mathrm{F}}Q_{\mathrm{F}})MN + (U_{\mathrm{O}} + U_{\mathrm{F}})M^2N\right)$
$f_\rho(\boldsymbol{x}^{(l)})$	$O\left((U_{\mathrm{O}}Q_{\mathrm{O}} + U_{\mathrm{F}}Q_{\mathrm{F}})MN\right)$
grad$f_\rho(\boldsymbol{x}^{(l)})$	$O(MN)$
$\mu^{(l)}$	$O(MN)$
Trans$\boldsymbol{d}^{(l-1)}$	$O(MN)$
$\boldsymbol{d}^{(l)}$	$O(MN)$
$\zeta^{(l)}$	$O(MN)$
$\boldsymbol{x}^{(l+1)}$	$O(MN)$

4 Numerical examples

In this section, we demonstrate the performance of our proposed RCG-CMDPC algorithm by implementing multiple numerical examples. First, we describe the setup experimental scenario and give the detailed parameters in Table 2. Then, we verify the effectiveness of the RCG-CMDPC algorithm under a typical DPJ scenario, and thereafter, the performance of our proposed algorithm is compared with that of a competing algorithm. Finally, we analyze the effect of the hyperparameters on the algorithm performance and present the Pareto curve of the RCG-CMDPC algorithm.

4.1 Setting of the experimental scenario

In the implemented experiment, we consider a typical scenario, which is consistent with the most advanced DPJ research (Yang ZP et al., 2024) for the convenience of subsequent comparison. The area of interest Ω is set as a 100 m×100 m square, wherein all the opponent equipment and three friendly devices are located. We set the center of Ω_{O} as the origin, i.e., (0 m, 0 m, 0 m), and the corresponding radius is r_{O}=5 m. The radii of Ω_{F}^1, Ω_{F}^2, and Ω_{F}^3 are all set as r_{F}=2 m, while their centers are located at (−20 m, 10 m, 0 m), (10 m, −20 m, 0 m), and (20 m, 25 m, 0 m), respectively. Within the area of interest Ω, the spatial grids are discretized as 1 m×1 m. The DPJ system is deployed above Ω at a distance d=2000 m, and the drones are assumed to be distributed randomly within a horizontal circle of radius 30 m, which is the same as in the work of Yang ZP et al. (2024). The carrier frequency is set as f_0=1 GHz, and the bandwidth and the length of the transmitted waveform

Table 2 Main settings of the typical DPJ scenario considered in this work

Symbol	Value	Meaning
Ω	100 m×100 m	Area of interest
Ω_{O}	(0 m, 0 m, 0 m)	Center of the opponent equipment
Ω_{F}^{1}	(−20 m, 10 m, 0 m)	Center of the friendly device 1
Ω_{F}^{2}	(10 m, −20 m, 0 m)	Center of the friendly device 2
Ω_{F}^{3}	(20 m, 25 m, 0 m)	Center of the friendly device 3
r_{O}	5 m	Radius of the opponent region
r_{F}	2 m	Radius of the three friendly regions
d	2000 m	Distance from DPJ system to the area of interest
f_0	1 GHz	Carrier frequency of the transmitted waveform
B	100 MHz	Bandwidth of the baseband jamming waveform
N	100	Length of the sampled waveform
Ξ_{O}	[950 MHz, 1050 MHz]	Potential working frequency of the opponent equipment
Ξ_{F}	[965 MHz, 1015 MHz]	Working frequency of the three friendly devices
p	30	L_p-norm approximation parameter
ε	10^{-5}	Stopping criterion of the RCG-CMDPC algorithm

are B=100 MHz and N=100, respectively. The potential working frequencies of the opponent and friendly devices are Ξ_{O}=[950 MHz, 1050 MHz] and Ξ_{F}=[965 MHz, 1015 MHz], respectively. Unless stated otherwise, we set p=30 for our RCG-CMDPC algorithm, and the stopping criterion is $\varepsilon=10^{-5}$. The experiments are conducted on a personal computer (PC) with an i7-10510U CPU and 16 GB RAM. For a clear understanding of our experiments, the above-stated main settings are listed in Table 2.

4.2 Verification of the effectiveness

In this subsection, we verify the effectiveness of our proposed RCG-CMDPC algorithm. Meanwhile, we compare the MM algorithm proposed by Yang ZP et al. (2024) with our algorithm in terms of DPJ performance and computational efficiency, which is the latest achievement of the wideband waveform design for DPJ. Note that the MM algorithm of Yang ZP et al. (2024) cannot be directly applied to our approximation problem $\tilde{\mathcal{P}}$ because the MM algorithm was proposed to tackle the L_p-norm approximation problem with CM continuous phase and the maximum CPS of friendly devices was considered as a constraint therein. In this case, we extend this MM algorithm to tackle our CM discrete-phase constrained problem $\tilde{\mathcal{P}}$, where the objective function $f_\rho(\boldsymbol{x})$ is majorized as discussed by Yang ZP et al. (2024), and the solution with CM and discrete phase constraints at each iteration is obtained as outlined by Bu et al. (2021). As shown in Figs. 3 and 4, we verify the DPJ effectiveness by the CPS distribution by adopting the MM and RCG-CMDPC algorithms for two cases, where case 1 is the typical DPJ scenario, and the working frequency of friendly devices is set the same as that of the opponent equipment in case 2. For these two cases, we set $\rho=10^{-10}$ in $\tilde{\mathcal{P}}$, and the effect of different V values on the final performance is also verified in these figures. It is seen that the two algorithms achieve the desirable jamming effect, where the red color represents that the corresponding spatial frequency grid has a high CPS level, and the blue color denotes a low CPS level. From the comparison, we find that the RCG-CMDPC algorithm performs better both on the minimum and the average CPSs of the opponent equipment than the MM algorithm, while the maximum CPSs of friendly devices using these two algorithms seem the same. The detailed CPS indicators of these two algorithms are shown in Table 3, where $\mathrm{CPS}_{\mathrm{O}}^{\min}$ and $\mathrm{CPS}_{\mathrm{O}}^{\mathrm{ave}}$ denote the minimum and average CPSs in Ω_{O}, respectively, while $\mathrm{CPS}_{\mathrm{F}}^{\max}$ and $\mathrm{CPS}_{\mathrm{F}}^{\mathrm{ave}}$ the maximum and average CPSs in Ω_{F}, respectively. We see that our proposed algorithm shows better performance on the CPS in Ω_{O}, and the MM algorithm has only a bit lower CPS in Ω_{F}, which can even be seen as the same as that of the RCG-CMDPC algorithm.

To further demonstrate the superiority of our proposed RCG-CMDPC algorithm, we give the convergence curves of the MM and RCG-CMDPC algorithms under the typical DPJ scenario, where the variation of

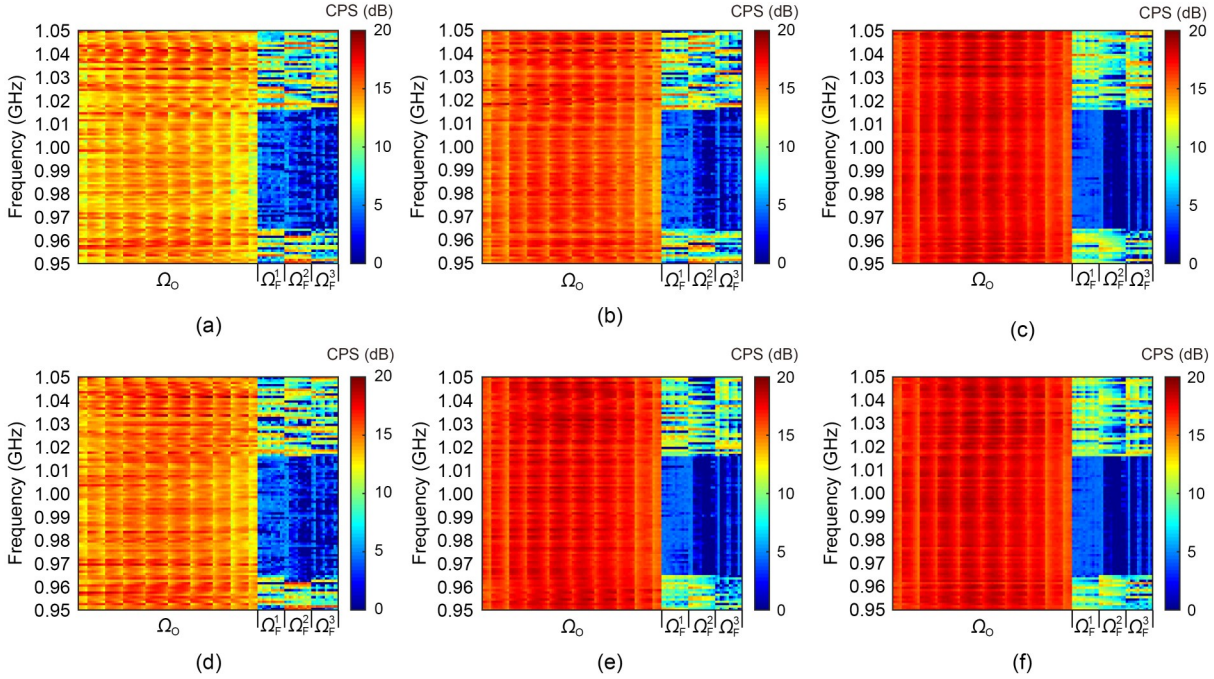

Fig. 3 Combined power spectrum (CPS) distribution in Ω_O and Ω_F with the adoption of different algorithms for case 1: (a) majorization–minimization (MM) algorithm (V=256; discrete phase); (b) MM algorithm (V=1024; discrete phase); (c) MM algorithm (V=∞; continuous phase); (d) Riemannian conjugate gradient for constant modulus discrete phase constraints (RCG-CMDPC) algorithm (V=256; discrete phase); (e) RCG-CMDPC algorithm (V=1024; discrete phase); (f) RCG-CMDPC algorithm (V=∞; continuous phase). References to color refer to the online version of this figure

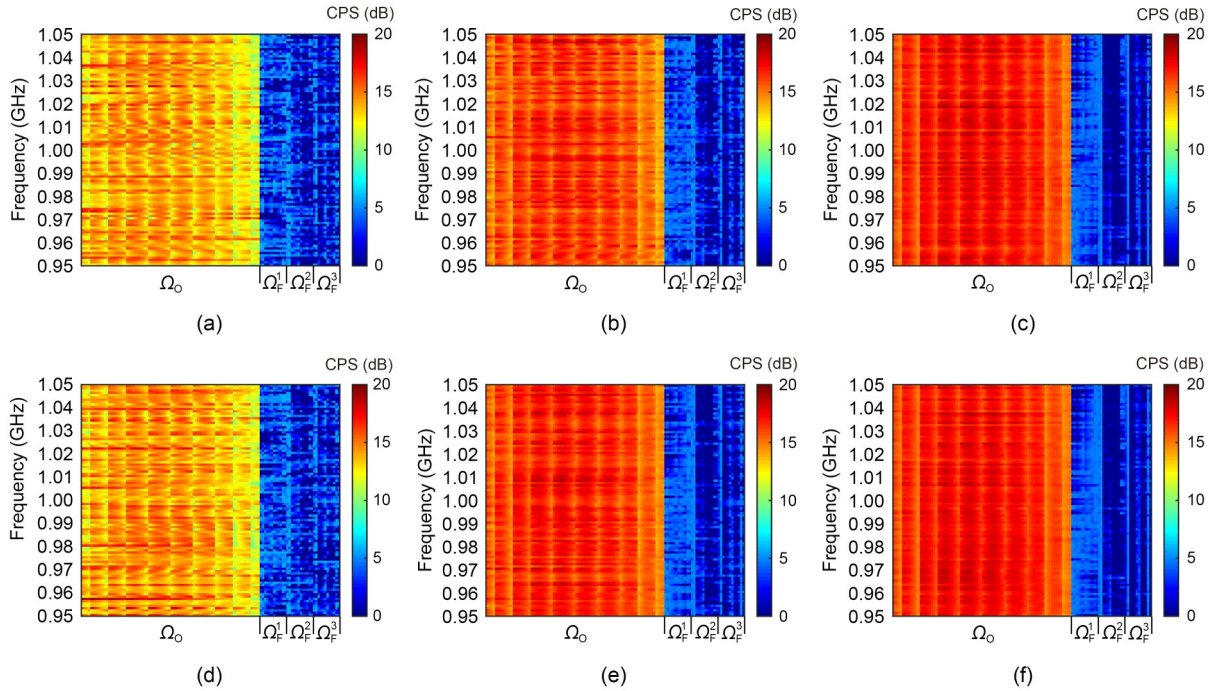

Fig. 4 CPS distribution in Ω_O and Ω_F with the adoption of different algorithms for case 2: (a) MM algorithm (V=256; discrete phase); (b) MM algorithm (V=1024; discrete phase); (c) MM algorithm (V=∞; continuous phase); (d) RCG-CMDPC algorithm (V=256; discrete phase); (e) RCG-CMDPC algorithm (V=1024; discrete phase); (f) RCG-CMDPC algorithm (V=∞; continuous phase). References to color refer to the online version of this figure

Table 3 CPS indicators in Ω_O and Ω_F for cases 1 and 2

V	Algorithm	CPS_O^{min} (dB) (case 1/2)	CPS_F^{max} (dB) (case 1/2)	CPS_O^{ave} (dB) (case 1/2)	CPS_F^{ave} (dB) (case 1/2)
256 (discrete phase)	MM	8.63/7.87	6.49/6.39	14.37/13.97	3.11/2.91
	RCG-CMDPC	11.20/8.79	6.30/6.29	15.08/14.24	3.02/3.00
1024 (discrete phase)	MM	12.92/12.78	5.68/5.70	15.97/15.93	3.04/2.70
	RCG-CMDPC	14.46/13.64	5.02/5.32	17.01/16.39	2.50/2.55
∞ (continuous phase)	MM	14.85/14.01	4.84/5.18	17.23/16.76	2.31/2.33
	RCG-CMDPC	15.03/14.12	4.82/5.17	17.37/16.81	2.35/2.77

$f_p(\boldsymbol{x})$ versus CPU time is given in Fig. 5. We observe that these curves decrease monotonically, which illustrates that both the MM and our proposed RCG-CMDPC algorithm converge well. From the comparison, we see that our proposed RCG-CMDPC algorithm has much better computational efficiency than the MM algorithm, with a decrease of about one order of magnitude in CPU time. The RCG-CMDPC algorithm obtains the corresponding discrete phase waveform efficiently, which makes it possible to generate real-time wideband waveform for DPJ. This superiority lies in the observation that the highest order of computational complexity of our algorithm is M^2N, while that of the MM algorithm is M^3N^3. Moreover, for the same algorithm, it is observed that the final objective decreases with increasing V. The reason is that a higher value of V provides a wider solution space for the approximation problem $\tilde{\mathcal{P}}$, and the discrete phase constraints are equivalent, to be consistent with the continuous phase scenario when $V=\infty$. From the above comparison, we conclude that the proposed algorithm achieves better CPS performance than the previous MM algorithm, and the computational efficiency is highly improved.

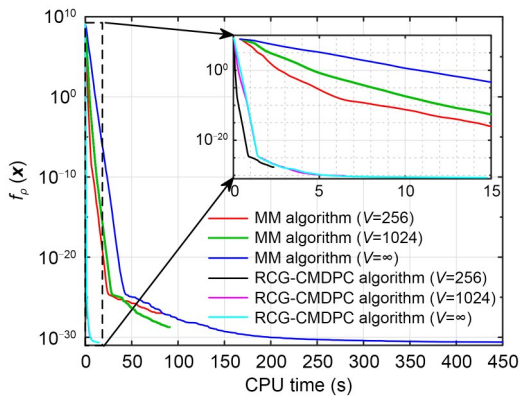

Fig. 5 Convergence curves of the MM and RCG-CMDPC algorithms

4.3 Performance analysis

To proceed, we analyze the effect of L_p-norm adoption on the performance of our proposed RCG-CMDPC algorithm. As shown in Fig. 6, we implement this experiment when V=1024, which means that each jammer is equipped with a 10-bit DDS. To investigate the effect of the value of p on the CPS performance and convergence of the algorithm, we set p=10, 20, 30, 40, and 50. From the curves, we see that the minimum CPS in Ω_O increases slightly with increasing p, while the maximum CPS in Ω_F tends to decrease as p increases. However, the convergence performance deteriorates severely when p is large, whereby the CPU time grows sharply in the figure. This phenomenon indicates that the CPS performance improvement is accompanied by the sacrifice of convergence and computational performance when adopting the L_p-norm approximation. It is explained by the fact that the L_p-norm with larger p values approximates the original (L_∞-norm) problem better.

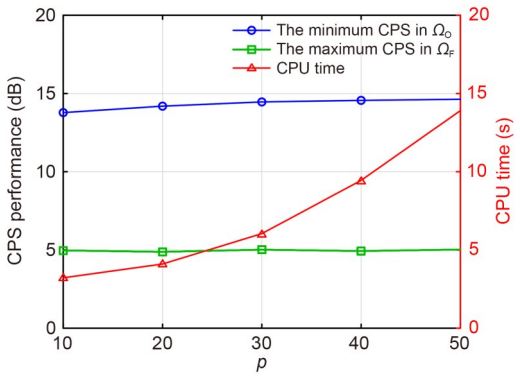

Fig. 6 Effect of value of p on the RCG-CMDPC algorithm performance

In what follows, we further analyze the effect of V on the convergence of our proposed RCG-CMDPC

algorithm. Fig. 7 depicts the variation of the objective function $f_\rho(\boldsymbol{x})$ versus the iteration index under different V values. From the comparison, it is seen that the final objective decreases with increasing V, where this value is far lower when V is >128. Meanwhile, the iteration index at the convergence highly increases, which means that the higher V value slows down the convergence of our RCG-CMDPC algorithm. It is explained by the fact that the higher V value results in a wider solution space, allowing the algorithm to obtain a better solution but inevitably requiring more iteration steps to the convergence. Specifically, we further give the analysis of the effect of V on the final CPS performance, where the minimum and maximum CPSs in Ω_{O} and Ω_{F} are shown by the curves in Fig. 8. These two CPS performances improve significantly when V grows no larger than 256. Moreover, when V is >1024, the achieved CPS performances in the discrete phase scenarios tend to be consistent with those in the continuous phase scenario.

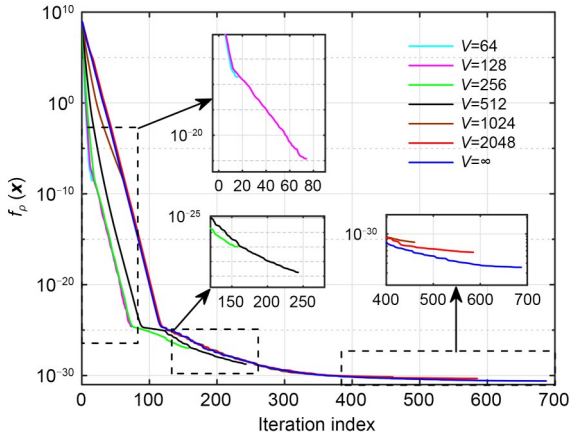

Fig. 7 Variation of $f_\rho(\boldsymbol{x})$ versus iteration index under different V values

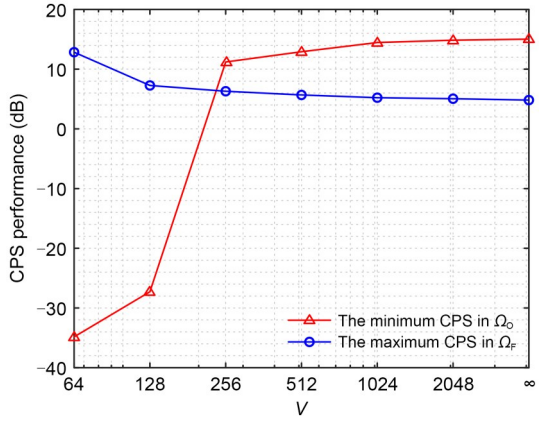

Fig. 8 Effect of V on the CPS performance of the RCG-CMDPC algorithm

Finally, we illustrate the impact of the parameter ρ on the CPS performance achieved using our proposed RCG-CMDPC algorithm. Specifically, the Pareto curves are obtained under three scenarios, where V= 256 and 1024 for the discrete phase scenario, and V= ∞ for the continuous phase scenario. Here, we set $\rho\in\{0,\rho_1,\rho_2,\cdots,\rho_{10},1\}\subseteq[0,1]$, where $\rho_i=10^{-55+5i}$, i= 1, 2, ⋯, 10. As marked in Fig. 9, when ρ=1 and 0, the obtained wideband waveform considers only Ω_{O} and Ω_{F}, respectively. Specifically, the higher the value of ρ, the better the minimum CPS in Ω_{O} and the worse the maximum CPS in Ω_{F} because the weight of this performance becomes higher in the formulated problem. This phenomenon is consistent with the Pareto theory as expected, which is a classical feature of bi-objective Pareto curves.

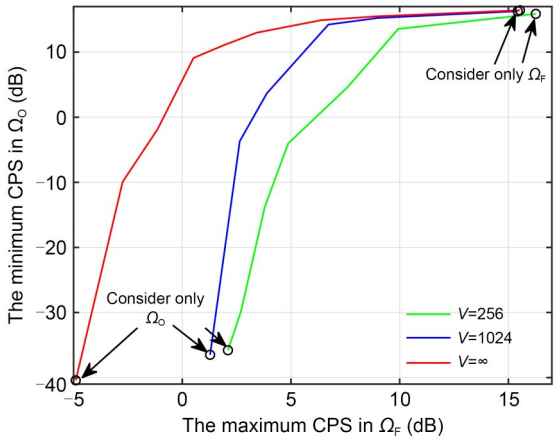

Fig. 9 Performance trade-off between the CPS in Ω_{O} and Ω_{F} under different V values

5 Conclusions

In this paper, we propose an efficient algorithm to design a robust wideband CM discrete phase waveform for DPJ, which aims to provide a robust DPJ effectiveness and low hardware burden on the jammers. The corresponding design model is formulated as a minimax MOP, which is transformed as $\tilde{\mathcal{P}}$ using the L_p-norm and Pareto framework. To tackle the challenging problem $\tilde{\mathcal{P}}$, we develop an efficient RCG-CMDPC algorithm within the RCG framework, whereby a novel

retraction and projection method is provided to let the solution satisfy the CM discrete phase constraints. The proposed RCG-CMDPC algorithm achieves a lower computational complexity than the competing MM algorithm in theory. The numerical examples show that the proposed algorithm has better CPS performance and computational efficiency than the MM algorithm, which makes it possible to design the real-time wideband CM discrete phase waveform for DPJ. Possible future works may include the robust wideband waveform design against the localization and synchronization errors of distributed UAVs.

Contributors

Qingsong ZHOU and Zhongping YANG designed the research. Jialong QIAN, Chao HUANG, Qinxian CHEN, Yibo XU, and Zhengkai WEI processed the data. Qingsong ZHOU and Jialong QIAN drafted the paper. Zhongping YANG helped organize the paper. Qingsong ZHOU, Jialong QIAN, and Zhongping YANG revised and finalized the paper.

Conflict of interest

All the authors declare that they have no conflict of interest.

Data availability

The data that support the findings of this study are available from the corresponding author upon reasonable request.

References

Absil P, Mahony R, Sepulchre R, 2008. Optimization Algorithms on Matrix Manifolds. Princeton University Press, Princeton, USA. https://doi.org/10.1515/9781400830244

Aubry A, De Maio A, Govoni MA, et al., 2020. On the design of multi-spectrally constrained constant modulus radar signals. *IEEE Trans Signal Process*, 68:2231-2243. https://doi.org/10.1109/TSP.2020.2983642

Blunt SD, Mokole EL, 2016. Overview of radar waveform diversity. *IEEE Aerosp Electron Syst Mag*, 31(11):2-42.

Boumal N, 2014. Optimization and Estimation on Manifolds. PhD Thesis, Université Catholique de Louvain, Leuven, Belgium.

Bu Y, Yu XX, Yang J, et al., 2021. A new approach for design of constant modulus discrete phase radar waveform with low WISL. *Signal Process*, 187:108145. https://doi.org/10.1016/j.sigpro.2021.108145

Chen SW, Xu CC, Zhang JY, 2020. Efficient focused energy delivery with grating lobe mitigation for precision electronic warfare. *Signal Process*, 169:107409. https://doi.org/10.1016/j.sigpro.2019.107409

Fan T, Yu XX, Gan N, et al., 2021. Transmit–receive design for airborne radar with nonuniform pulse repetition intervals. *IEEE Trans Aerosp Electron Syst*, 57(6):4067-4084. https://doi.org/10.1109/TAES.2021.3090915

Fan T, Cui GL, Yu XX, et al., 2024. Joint design of intra–inter agile pulses and Doppler filter banks for Doppler ambiguous target. *IEEE Trans Signal Process*, 72:867-882. https://doi.org/10.1109/TSP.2024.3355768

Gao J, Wu RH, Zhang JD, 2020. An adaptive multi-target jamming waveform design based on power minimization. *Entropy*, 22(5):508. https://doi.org/10.3390/e22050508

Geng J, Jiu B, Li K, et al., 2023. Radar and jammer intelligent game under jamming power dynamic allocation. *Remote Sens*, 15(3):581. https://doi.org/10.3390/rs15030581

Imani S, Nayebi MM, 2021. A coordinate descent framework for beampattern design and waveform synthesis in MIMO radars. *IEEE Trans Aerosp Electron Syst*, 57(6):3552-3562. https://doi.org/10.1109/TAES.2021.3074207

Kelsey PW, 2023. A pulse-on-pulse technique for electronic warfare systems. *IEEE Trans Aerosp Electron Syst*, 59(6): 9769-9774. https://doi.org/10.1109/TAES.2023.3285518

Li J, Stoica P, 2008. MIMO Radar Signal Processing. Wiley, Hoboken, USA. https://doi.org/10.1002/9780470391488

Liu RT, Zhang W, Yu XX, et al., 2022. Transmit–receive beamforming for distributed phased-MIMO radar system. *IEEE Trans Veh Technol*, 71(2):1439-1453. https://doi.org/10.1109/TVT.2021.3133596

Lu JH, Fan T, Yu XX, et al., 2021. Robust design and evaluation of phase codes for radar performance optimization with a finite alphabet constraint. *Electron Lett*, 57(10):415-418. https://doi.org/10.1049/ell2.12146

Manton JH, 2020. Geometry, manifolds, and nonconvex optimization: how geometry can help optimization. *IEEE Signal Process Mag*, 37(5):109-119. https://doi.org/10.1109/MSP.2020.3004034

Pärlin K, Riihonen T, Le Nir V, et al., 2021. Full-duplex tactical information and electronic warfare systems. *IEEE Commun Mag*, 59(8):73-79. https://doi.org/10.1109/MCOM.001.2001139

Pishrow MM, Abouei J, 2021. Joint design of the discrete phase transmit sequence and receive filter in radar systems. *IET Radar Sonar Nav*, 16(2):315-326. https://doi.org/10.1049/rsn2.12185

Qiu XF, Zhang XY, Huo K, et al., 2023. Quartic Riemannian adaptive regularization with cubics for radar waveform design. *IEEE Trans Aerosp Electron Syst*, 59(6):7514-7528. https://doi.org/10.1109/TAES.2023.3289779

Shi MD, Li XH, Liu JW, et al., 2024. Constant modulus waveform design for RIS-aided ISAC system. *IEEE Trans Veh Technol*, 73(6):8648-8659. https://doi.org/10.1109/TVT.2024.3362431

Song D, Wang W, Xu ZH, et al., 2016. Focused energy delivery with protection for precision electronic warfare. *IEEE Trans Aerosp Electron Syst*, 52(6):3053-3064. https://doi.org/10.1109/TAES.2016.150713

Song JX, Babu P, Palomar DP, 2016. Sequence design to minimize the weighted integrated and peak sidelobe levels. *IEEE Trans Signal Process*, 64(8):2051-2064. https://doi.org/10.1109/TSP.2015.2510982

Song YX, Wang Y, Xie JY, et al., 2022. Ultra-low sidelobe waveforms design for LPI radar based on joint complementary phase-coding and optimized discrete frequency-coding.

Remote Sens, 14(11):2592. https://doi.org/10.3390/rs14112592

Tai N, Cui KB, Wang C, et al., 2016. The design of a novel coherent noise jammer against LFM radar. *IEICE Electron Expr*, 13(21):20160924. https://doi.org/10.1587/elex.13.20160924

Tan R, Bu Y, Pan BN, et al., 2024. Cooperative waveforms design for distributed sites in multiple blanket jamming. *IEEE Sens J*, 24(6):8774-8787. https://doi.org/10.1109/JSEN.2024.3359601

Wang YX, Huang GC, Li W, 2018. Waveform design for radar and extended target in the environment of electronic warfare. *J Syst Eng Electron*, 29(1):48-57. https://doi.org/10.21629/JSEE.2018.01.05

Wu QH, Zhao F, Zhao TH, et al., 2023. Stepped frequency chirp signal imaging radar jamming using two-dimensional nonperiodic phase modulation. *Front Inform Technol Electron Eng*, 24(3):433-446. https://doi.org/10.1631/FITEE.2200298

Xu YB, Huang C, Zhang CD, et al., 2022, A fast jamming waveform design method based on distributed precision jamming. Proc 2nd Int Conf on Computer Science, Electronic Information Engineering and Intelligent Control Technology, p.94-98. https://doi.org/10.1109/CEI57409.2022.9950158

Yang J, Aubry A, De Maio A, et al., 2022. Multi-spectrally constrained transceiver design against signal-dependent interference. *IEEE Trans Signal Process*, 70:1320-1332. https://doi.org/10.1109/TSP.2022.3144953

Yang J, Tan YS, Yu XX, et al., 2023. Waveform design for watermark framework based DFRC system with application on joint SAR imaging and communication. *IEEE Trans Geosci Remote Sens*, 61:5200214. https://doi.org/10.1109/TGRS.2022.3232528

Yang ZP, Zhou QS, Li ZH, et al., 2021. Grating lobe suppression in focussed energy delivery for precision electronic warfare. *IET Radar Sonar Nav*, 15(11):1420-1432. https://doi.org/10.1049/rsn2.12134

Yang ZP, Yang SN, Zhou QS, et al., 2022. A joint optimization algorithm for focused energy delivery in precision electronic warfare. *Defence Technol*, 18(4):709-721. https://doi.org/10.1016/j.dt.2021.03.001

Yang ZP, Zhang BY, Zhang KD, et al., 2023. Efficient waveform design with jamming characteristics for precision electronic warfare. *Signal Process*, 212:109162. https://doi.org/10.1016/j.sigpro.2023.109162

Yang ZP, Li ZH, Yu XX, et al., 2024. Maximin design of wideband constant modulus waveform for distributed precision jamming. *IEEE Trans Signal Process*, 72:1316-1332. https://doi.org/10.1109/TSP.2024.3365940

Zeng CC, Wang FZ, Li HB, et al., 2023. Target detection for distributed MIMO radar with nonorthogonal waveforms in cluttered environments. *IEEE Trans Aerosp Electron Syst*, 59(5):5448-5459. https://doi.org/10.1109/TAES.2023.3260819

Zhang JD, Xu NQ, 2020. Discrete phase coded sequence set design for waveform-agile radar based on alternating direction method of multipliers. *IEEE Trans Aerosp Electron Syst*, 56(6):4238-4252. https://doi.org/10.1109/TAES.2020.2993683

Zhang KD, Wang J, Zhou QS, et al., 2022a. Jamming waveform designed in focused energy delivery for precision electronic warfare scenario. Proc 7th Int Conf on Intelligent Computing and Signal Processing, p.1382-1386. https://doi.org/10.1109/ICSP54964.2022.9778715

Zhang KD, Zhou QS, Wang J, et al., 2022b. A method for jamming waveform design in precision electronic warfare scenarios. *IET Signal Process*, 16(5):562-574. https://doi.org/10.1049/sil2.12126

Zhang KD, Zhou QS, Wang J, et al., 2023. Wideband waveform design for distributed precision jamming. *Entropy*, 25(3): 496. https://doi.org/10.3390/e25030496

Zhang WJ, Hu JF, Wei ZY, et al., 2020. Constant modulus waveform design for MIMO radar transmit beampattern with residual network. *Signal Process*, 177:107735. https://doi.org/10.1016/j.sigpro.2020.107735

Zhao LC, Song JX, Babu P, et al., 2017. A unified framework for low autocorrelation sequence design via majorization–minimization. *IEEE Trans Signal Process*, 65(2):438-453. https://doi.org/10.1109/TSP.2016.2620113